

OPEN ACCESS

## Understanding Adverse Effects of Temperature Shifts on Li-Ion Batteries: An Operando Acoustic Study

To cite this article: Wesley Chang *et al* 2020 *J. Electrochem. Soc.* **167** 090503

View the [article online](#) for updates and enhancements.

### ECS Toyota Young Investigator Fellowship

For young professionals and scholars pursuing research in batteries, fuel cells and hydrogen, and future sustainable technologies.

At least one \$50,000 fellowship is available annually.  
More than \$1.4 million awarded since 2015!



Application deadline: January 31, 2023



TOYOTA

**Learn more. Apply today!**



# Understanding Adverse Effects of Temperature Shifts on Li-Ion Batteries: An Operando Acoustic Study

Wesley Chang,<sup>1,2,3,\*</sup> Clement Bommier,<sup>1,2,3,=</sup> Thomas Fair,<sup>1,2</sup> Justin Yeung,<sup>1,2</sup> Shripad Patil,<sup>4,\*</sup> and Daniel Steingart<sup>1,2,3,4,5,6,z</sup>

<sup>1</sup>Department of Mechanical and Aerospace Engineering, Princeton University, Princeton, New Jersey 08540, United States of America

<sup>2</sup>Andlinger Center for Energy and the Environment, Princeton University, Princeton, New Jersey 08540, United States of America

<sup>3</sup>Columbia Electrochemical Energy Center, Columbia University, New York, New York 10027, United States of America

<sup>4</sup>Department of Earth and Environmental Engineering, Columbia University, New York, New York 10027, United States of America

<sup>5</sup>Department of Chemical Engineering, Columbia University, New York, New York 10027, United States of America

<sup>6</sup>Department of Chemical and Biological Engineering, Princeton University, Princeton, New Jersey 08540, United States of America

Studies related to battery performance and long-term health of commercial Li-ion batteries (LIBs) typically have a fixed temperature parameter. However, commercial LIBs are subject to temperature fluctuations due to their local environment and operating conditions, and these transient temperatures are well known to impact long-term stability. Herein, we demonstrate the adverse effects of temperature shifts, and show that transitioning from low temperature to higher temperature can lead to catastrophic failure within practical temperature ranges experienced by commercial LIBs. We show there exists an Arrhenius relationship between the rate of acoustic attenuation and the magnitude of the temperature shift. A combination of acoustic attenuation, which marks gassing occurrence during cycling, and post mortem chemical analyses provides further mechanistic insight into the Li-rich solid electrolyte interphase (SEI) formation at low temperatures and subsequent reactions with the electrolyte at higher temperatures. Further, several strategies to prevent or mitigate catastrophic failure are introduced. On a broader scale, this research further highlights the importance of temperature and current controls integration into battery management systems (BMS) for both safety and extension of cycle life as battery systems move toward fast charge (>3 C) capability.

© 2020 The Author(s). Published on behalf of The Electrochemical Society by IOP Publishing Limited. This is an open access article distributed under the terms of the Creative Commons Attribution 4.0 License (CC BY, <http://creativecommons.org/licenses/by/4.0/>), which permits unrestricted reuse of the work in any medium, provided the original work is properly cited. [DOI: 10.1149/1945-7111/ab6c56]



Manuscript submitted October 7, 2019; revised manuscript received November 27, 2019. Published February 6, 2020. *This paper is part of the JES Focus Issue on Battery Safety, Reliability and Mitigation.*

Supplementary material for this article is available [online](#)

Temperature contributions to aging mechanisms of commercial lithium-ion batteries (LIBs) are generally focused on the harmful high temperature effects, such as electrolyte decomposition and cathode dissolution at >60 °C, and deleterious low temperature effects, arising from lithium plating on the anode surface during charging (generally below 10 °C).<sup>1–16</sup> In parallel, researchers have also explored temperature abuse and failure pathways of LIBs due to thermal runaway, through means of overcharge and calorimetry.<sup>17–23</sup>

However, these studies seldom consider the effect of temperature shifts, and in the case of abuse and overcharge, operate well outside manufacturer specifications, thus limiting insight into aging mechanisms under standard operating conditions. LIBs are expected to cycle in environments with changing temperatures, with greater temperature margins in polar regions due to extreme seasonal variations. This is an important consideration to take into account for the building of battery management systems (BMS) in outdoor environments, such as mobility applications (i.e. electric vehicles, electric bikes) and grid-level storage; adaptability to temperature swings in the operating environment is critical. The same is true for batteries used in space and in remote sensing applications, where fluctuations are even more extreme.

Recently, Dahn et al. demonstrated cell failure stemming from gassing effects during a cold to hot temperature transition.<sup>24</sup> Volume analysis quantified the volume increase that occurs when lithium plating is observed during cycling at 10 °C in ethylene carbonate-free electrolytes. This work aims to establish a mechanistic understanding of temperature shift effects on gassing. Through a combination of

operando acoustic detection and material characterization techniques, we demonstrate that LiCoO<sub>2</sub>/graphite LIBs (LCO/Gr) experience catastrophic battery failure when moved from a 0 °C environment to a 60 °C environment during cycling. The temperature range of 0 °C to 60 °C was chosen based on the manufacturer specification sheet for minimum and maximum operating temperatures (linked in Experimental Methods section). By shifting the environmental temperature between the minimum and maximum operating extremes and at a control temperature of 20 °C, which is the baseline environment utilized for manufacturer performance testing, the catastrophic failure events that could possibly happen even within accepted ranges could be investigated. Further, it is known that lithium plates readily on graphite below 10 °C at typical 1C charge rates, and that LiPF<sub>6</sub> electrolyte decomposition beings to occur at 60 °C and higher.<sup>1,4,10,16</sup> For all these reasons, it made sense to select these two temperature ranges for the temperature shift experiments.

From the experimental results, the catastrophic failure in the 0 °C to 60 °C temperature shift stems from a two-step process: lithium deposition at 0 °C, and subsequent electrolyte gassing reactions at high temperature (greater than 20 °C) which we determine to be catalyzed by the prior lithium deposition. This results in overall failure of the battery within ten cycles post-temperature-shift, showing how critical it is to manage current rate as a function of temperature, especially for battery applications which require operation in fluctuating temperatures. We further demonstrate that heating the cycling environment to any temperature above 20 °C, after initial cycling in <10 °C, results in catastrophic failure of the battery, even if the battery is held at rest at 0% state-of-charge. This is shown by an Arrhenius relationship between the magnitude of temperature shift and the time it takes the acoustic signal to fully attenuate. Ultrasonic signals transmitted through the battery provide evidence of when gassing occurs, because ultrasonic waves are

\*Electrochemical Society Member.

=These authors contributed equally to this work.

<sup>z</sup>E-mail: [dan.steingart@columbia.edu](mailto:dan.steingart@columbia.edu)

dramatically attenuated in the presence of a gaseous medium due to a high acoustic impedance mismatch. Finally, we explore several possible strategies for preventing catastrophic failure from occurring due to the temperature shift.

### Experimental Methods

**Li-ion pouch cell cycling.**—Cells used for testing were Li-ion 651628 (LCO/Gr) pouch cells, rated for 210 mAh, and obtained from AA Portable Power Corp. (<https://batteryspace.com/prod-specs/4252.pdf>). Detailed chemical composition information is shown in Table I (from the company specification sheet).

Cell properties in Table II were obtained by reverse-engineering a fresh cell at 0% state-of-charge. There were 30 cathode (LCO) layers and 32 anode (graphite) layers, with each electrode being double-sided. The LCO electrodes were sonicated in NMP, and the graphite electrodes were sonicated in DI water. The slurry was dried in the vacuum oven at 150 °C overnight in order to obtain the dried powder. The weight of the powder was measured to obtain the loading ( $\text{mg cm}^{-2}$ ) and density ( $\text{g cm}^{-3}$ ). Areal capacity was obtained using the theoretical capacity of 274 mAh  $\text{g}^{-1}$  for LCO and 372 mAh  $\text{g}^{-1}$  for graphite. BET measurements (Micromeritics ASAP 2020 HV) were taken for both the LCO and graphite in order to obtain the BET surface area and micropore volume.

Cells were cycled on a Neware BTS3000 cycler, using constant current constant voltage (CCCV) on the charge step and constant current (CC) on the discharge step. For the CCCV tests, the lower current cutoff was always C/10. The voltage window used was between 2.7 V and 4.2 V, consistent with factory specified cut-off voltages. Cycling was done in environments between 0 °C and 60 °C in temperature-controlled incubators. The nominal capacity was established by cycling batteries at a C/10 rate at CC.

Galvanostatic intermittent titration (GITT) testing was conducted to compare relative diffusivity values during the electrochemical cycling processes, in a process first described by Weppner et al.<sup>25</sup> and shown to be functional for porous LIB electrodes by Dees et al.<sup>26</sup> Diffusivity measurements were obtained through the use of Eq. 1.

$$\tilde{D} = \frac{4}{\pi\tau} \left( \frac{m_B V_M}{M_B S} \right)^2 \left( \frac{\Delta E_s}{\Delta E_t} \right)^2 \left( t \ll \frac{L^2}{\tilde{D}} \right) \quad [1]$$

For the full cells, a current pulse of C/10 with a transient current time of 10 min and a resting period of 40 min was used. From the voltage stability observed in the voltage curves, 40 min was determined to be an appropriate rest time to attain steady stage following the 10 min C/10 pulse.

**Acoustic monitoring.**—Acoustic ultrasound is used as a tool to measure the time-of-flight (ToF) of a waveform passing through a cell. The ToF can be obtained by the cell thickness L, divided by the

speed of sound  $C_s$ , with the speed of sound being a function of the elastic modulus of the material, E, as well as the density  $\rho$  (Eq. 2).

$$\text{ToF} = \frac{L}{C_s} = \frac{L}{\sqrt{E/\rho}} \quad [2]$$

According to acoustic theory, the transmission efficiency from transducer to air is much lower than that from transducer to liquid, due to a greater impedance mismatch ratio. Therefore, the loss or complete attenuation of the acoustic signal should be indicative of gassing within the pathway between the transmitting and receiving transducers. Individual waveforms are collated via superposition onto a heatmap to show their evolution over time. ToF shifts are determined using a full waveform cross-correlation function. More information on the technique, as well as more advanced analysis is available in papers by Steingart et al.<sup>27–29</sup> and Shearing et al.<sup>22</sup> The acoustic signal was transmitted and received by a pair of 2.25 MHz transducers (SIUI) that were contacted across the cell, with the signal collected by an ultrasonic pulser-receiver (Epoch 600). Coupling of the acoustic signal to the cell was applied via an acoustic gel (Sonogel), and transducer pressure was maintained via springs in a custom 3D printed holder (Formlabs) (SI Fig. 1 is available online at [stacks.iop.org/JES/167/090503/mmedia](https://stacks.iop.org/JES/167/090503/mmedia)).

**Materials characterization.**—Scanning electron microscopy (SEM) was conducted using a Verios 460 XHR with a working distance of 4 mm and accelerating voltage of 5 keV. Samples were rinsed in dimethyl carbonate and dried in the vacuum antechamber of the Argon filled glovebox at 40 °C for 2 h before imaging. Samples were transferred to the imaging room in double sealed containers and were exposed to air for less than 5 s, using the load lock on the SEM for near-instant pump down. X-ray photoelectron spectroscopy (XPS) was conducted using a Thermo Scientific K-Alpha instrument with an Al K $\alpha$  source and 400  $\mu\text{m}$  spot size (0.05 eV step size for core-level scans, 1 eV for survey scans). The operating pressure was less than  $1 \times 10^{-7}$  Torr, and the samples were transferred via a vacuum sample holder and never exposed to atmosphere. Advantage software was used for the least-squares fitting of XPS spectra with Lorentzian-Gaussian line shape (30% L/G mix), and a Shirley background subtraction. Depth profiling was carried out with an Argon ion gun (2 keV, monatomic, 400  $\mu\text{m}$  spot size) for a series of 7 etches of 180 s each (21 min total). Raman analysis was done with a Horiba Raman Spectrometer, using a 532 nm laser. A glass fiber filter paper was used for greater electrolyte retention, before analysis. FTIR was conducted using a Nicolet iN10 MX Infrared Microscope.

### Results and Discussion

**Temperature shift effects during cycling.**—While battery manufacturers generally recommend LIB operation and storage at temperatures between 20 °C and 30 °C, it is common for batteries to be placed in environments which deviate from those guidelines. Therefore, the aim of this work was to explore the effect of temperature shifts between the absolute minimum and maximum manufacturer specified temperatures. For the case of the LIB chosen for this study, the minimum and maximum temperature range was 0 °C to 60 °C, with baseline performance testing completed at 20 °C. The effect of shifting the battery between these temperature environments on lifetime cycling was first investigated.

Six batteries were cycled with various permutations of a 5 °C/20 °C/60 °C temperature profile, with 30 cycles at each temperature followed by a final 30 cycle step at 20 °C (Fig. 1a). Each cycle consisted of a CCCV charge to 4.2 V cutoff, and a CC discharge to 2.7 V cutoff. While five of the permutations appear to perform consistently, the low to high temperature transition (5 °C/60 °C/20 °C) was a condition that warranted further investigation. Not only did it fail completely after cycling at 60 °C, but it showed physical signs of severe gassing (Fig. 1c). The gassing phenomenon is typical of overcharging or exposure to higher temperatures. However, none

**Table I. Chemical Composition.**

Chemical Name	Content (wt%)	CAS Index No
Lithium cobalt oxide	50	12190-79-3
Graphite	10	7782-42-5
Polypropylene	5	9003-07-0
PVDF	2	24937-79-9
Polyethylene	5	9002-88-4
Carboxymethylcellulose	0.5	9004-32-4
Lithium hexafluorophosphate	5	21324-40-3
Ethylene carbonate	5	96-49-1
Dimethylcarbonate	5	616-38-6
Nickel	2.5	7440-02-0
Copper	5	7440-50-8
Aluminum	5	7429-90-5

Table II. Cell Properties.

	Electrode	# Layers	Thickness (um)	Loading (mg cm <sup>-2</sup> )	Density (g cm <sup>-3</sup> )
<b>LCO</b>	Cathode	30	58	8.9	1.54
<b>Graphite</b>	Anode	32	66	7.0	1.06
	Capacity (mAh cm <sup>-2</sup> )		BET Surface Area (m <sup>2</sup> g <sup>-1</sup> )		BET Micropore Volume (cm <sup>3</sup> g <sup>-1</sup> )
<b>LCO</b>	2.44		2.45		0.000753
<b>Graphite</b>	2.60		3.18		0.000214

of the cells were overcharged to greater than 4.2 V, and since the other cells were also exposed to higher temperature (yet none showed significant signs of gassing or cell failure), it was suspected that the low temperature to high temperature shift affected the electrochemical properties which led to cell failure.

To confirm the capacity degradation observed in the low to high temperature shift, the low to high temperature shift cycling test was replicated with four cells, cycled from 0 °C to 60 °C. As observed in Fig. 1b, all four cells lose a significant amount of capacity during their cycling at 0 °C—as had been expected, and is similar to findings by Matadi et al.<sup>30</sup> and Dahn et al.<sup>24</sup> who ascribed the loss to Li deposition and SEI formation in the pores of the anode. When the transition to 60 °C was made, each showed signs of capacity increase, followed by immediate fading. The gains in capacity afforded by the shift to higher temperature cycling are only temporary, and all cells show signs of capacity decline in subsequent cycles. Moreover, all cells show visual evidence of internal gassing once moved to higher temperatures, observed by significant bulging of the pouch cell (Fig. 1c).

**Temperature shift effects during open circuit potential.**—As shown, low (<10 °C) to high (60 °C) temperature shifts during cycling lead to capacity loss greater than 80% of expected capacity

as well as substantial gas formation, presumably due to reactions induced by the temperature shift. To further explore and understand the dependence of gas formation on temperature gradients and the root cause of the gassing occurrence, fresh 210 mAh pouch cells were initially cycled at cold (<10 °C) temperatures at 1C rate to induce plating, before the environment was shifted to a higher temperature, while keeping the cells at bottom-of-charge and open circuit potential. Results were compared for shifts to 20 °C, 30 °C, 40 °C, 50 °C, and 60 °C. Operando acoustic ultrasound was utilized to detect gassing, which would fully attenuate an acoustic signal due to a high acoustic impedance mismatch.<sup>27–29</sup>

Since the cells were kept at 0% SOC and open circuit potential, effects of electrolyte degradation at higher SOC and during cycling should be mitigated. Therefore, any cell degradation should be primarily an effect of the higher temperature environment in combination with the initial effects of cold temperature cycling. Since gassing reactions should be minimized if electrolyte degradation is indeed a primary contributor to gas formation, the cells were expected to retain the acoustic transmission during the transition from cold to hot temperature. There would be a slight hysteresis in the time-of-flight since warmer temperatures invariably cause a change in the Young's modulus, leading to different transmission of sound for the materials within the battery. However, signal

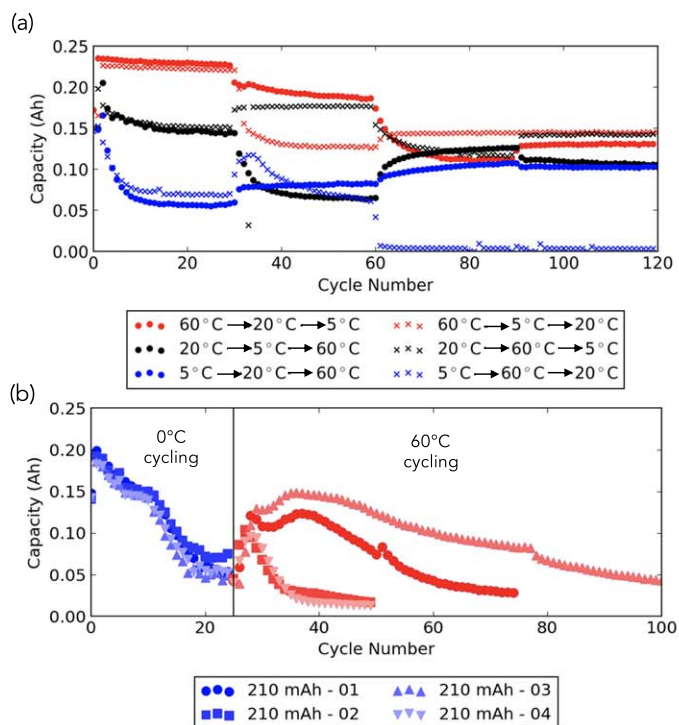


**Figure 1.** (a) Initial cycling of 210 mAh cells following six different temperature permutation profiles at temperatures of 5 °C, 20 °C and 60 °C. 30 cycles were achieved at each temperature, with the last remaining 30 cycles at 20 °C. Constant current constant voltage (CCCV) cycling protocol was utilized, with a current rate of 1C and a cutoff current of C/10. (b) Four different pouch cells cycled at the same condition: 0 °C for 25 cycles, followed by a shift to 60 °C, and 70 cycles at 60 °C. (c) Optical images of a 210 mAh pouch cell following cycling at 0 °C (left), and following cycling after shifting to 60 °C with cell failure and signs of gassing (right). The scale bar in (c) corresponds to 1 cm.



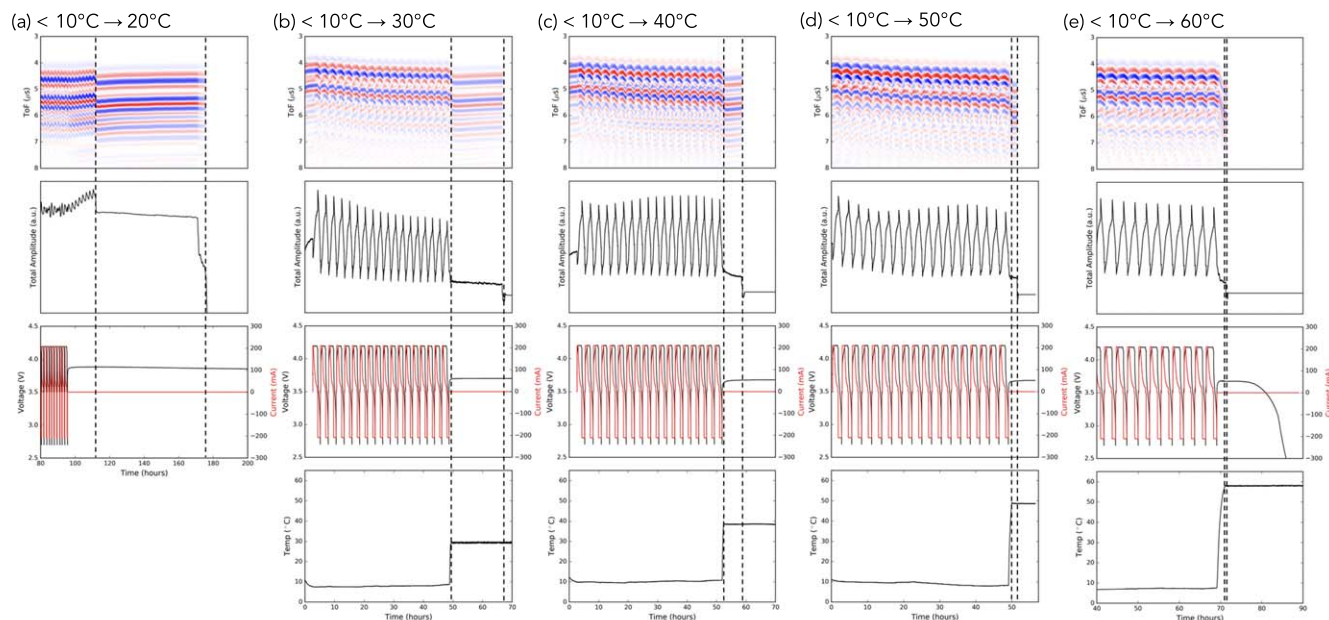


**Figure 2.** Acoustic and electrochemical data of 210 mAh pouch cells initially cycled at cold ( $<10^{\circ}\text{C}$ ) temperature to induce plating, before the environmental temperature was shifted higher to (a)  $20^{\circ}\text{C}$ , (b)  $30^{\circ}\text{C}$ , (c)  $40^{\circ}\text{C}$ , (d)  $50^{\circ}\text{C}$ , and (e)  $60^{\circ}\text{C}$  while keeping the cell at open circuit potential and bottom-of-charge. For each condition, plots are shown for the heatmap of the acoustic waveforms superimposed over time on the x-axis (the acoustic time-of-flight), the total amplitude vs time, the voltage/current profiles, and the environmental temperature in the incubator as measured by a thermistor. The dotted lines indicate the time range starting from the temperature shift, until loss of signal was observed.

attenuation was observed for all temperature shifts, as described in the next section.

Figure 2 depicts the acoustic signal transmission for all temperature shift profiles examined. Each cell was initially cycled at 1C rate (CCCV charge to 4.2 V, CC discharge to 2.7 V) at a temperature of  $<10^{\circ}\text{C}$ , before the temperature was shifted higher while the cell was held at open circuit potential at the end of the last discharge. This initial cycling can be observed by the initial cyclical trends in the superimposed acoustic time-of-flight (ToF), with ToF increasing on charge and decreasing on discharge. This has been shown before to arise from the dominant acoustic effects of the graphite anode modulus, with the local inflection points due to graphite staging events.<sup>28</sup> As described earlier, the initial temperature shift, shown by the first dotted line, results in a corresponding shift of the acoustic waveforms due to temperature effects on sound transmission. Subsequently, acoustic signal loss was observed for all temperature shifts. For the shift to the maximum operating temperature of  $60^{\circ}\text{C}$ , the signal loss occurred immediately after the temperature shift, in less than one hour (Fig. 2e). For the shift to  $20^{\circ}\text{C}$ , the signal loss occurred approximately 63 h after the temperature shift (Fig. 2a). For the shifts to  $30^{\circ}\text{C}$ ,  $40^{\circ}\text{C}$ , and  $50^{\circ}\text{C}$ , the signal loss occurred 14.7 h (Fig. 2b), 6.7 h (Fig. 2c), and 1.6 h (Fig. 2d) after the temperature shift. These losses in signal are also reflected in the second subplots of Fig. 2, where the total amplitude remains stable after the temperature shift before quickly attenuating after an amount of time. The attenuation was shown to be independent of the gain used in the acoustic pulse, as a lower decibel pulse of 30 dB or higher pulse of 70 dB both showed signal attenuation at the same time. This confirms that the signal is affected by an internal event, as opposed to extrinsic acoustic factors (SI Fig. 2).

Whereas the signal for  $0^{\circ}\text{C}$  to  $20^{\circ}\text{C}$  took approximately 63 h to attenuate (Fig. 2a), the signal from the  $0^{\circ}\text{C}$  to  $60^{\circ}\text{C}$  transition disappears within 1 hour of the transition (Fig. 2e). When the transition is first made (first dotted line), there is an immediate increase in the ToF, as was observed with the  $0^{\circ}\text{C}$  to  $20^{\circ}\text{C}$  transition. The ToF continues to increase until an abrupt disappearance within an hour of transitioning to  $60^{\circ}\text{C}$ . This is in contrast to the  $20^{\circ}\text{C}$  case, where the ToF remains relatively constant after the temperature is shifted. The other noticeable difference that is spotted

between the shift to  $20^{\circ}\text{C}$ , and the shift to  $60^{\circ}\text{C}$  is the behavior of the open circuit potential. In the shift to  $20^{\circ}\text{C}$ , the potential stays constant for the duration of the observation period. However, in the shift to  $60^{\circ}\text{C}$ , the potential undergoes a significant decrease to 0 V, suggesting complete cell failure (last plot of Fig. 2e).

The observed effects of temperature shifts during rest provide insight into the continuum effects of plating and gassing in a battery. Lower temperatures, especially below  $10^{\circ}\text{C}$  at 1C cycling rates, increase the tendency for Li plating to occur due to lower Li diffusivity.<sup>1,4,10,16</sup> Higher temperatures increase Li diffusivity, but also speed up electrolyte decomposition reactions. The presence of Li plating would change the degree and type of decomposition reactions occurring. As demonstrated, the gassing and complete cell failure at  $60^{\circ}\text{C}$  was also observed for the lower temperature shifts but to a lesser degree. In order to visualize the temperature dependence of the Li plating-induced gassing decomposition reactions, the rate of signal attenuation was measured and plotted against the magnitude of the temperature shift, as demonstrated in Fig. 3. The rate is defined by the inverse of the signal attenuation time. The temperature is measured to be the magnitude of the temperature shift. To carefully demonstrate the Arrhenius relation of these parameters, signal attenuation was defined by the drop in amplitude below the local minima, and the initial time was calculated to be the point at which the higher temperature was reached as measured by the thermistor (these are shown by the two vertical dotted lines in Fig. 2 subplots). In the appropriate Arrhenius relationship format, we observe a statistically significant linear trend with correlation coefficient of 99.6%. The signal attenuation time proves here to be a very good indicator of when gassing would occur at a given temperature shift, within the ranges of practical operating temperatures.

For the two extremes (shift to  $20^{\circ}\text{C}$  and shift to  $60^{\circ}\text{C}$ ), further cycling and diffusivity measurements were taken. After the shift to higher temperatures and the long hold, the cells were then cycled at the baseline temperature of  $20^{\circ}\text{C}$ , at 1C rate and CCCV. The  $20^{\circ}\text{C}$  shifted cell was able to cycle with a capacity of 0.09 Ah, before falling to 0.05 Ah after 100 cycles (SI Fig. 3a). Meanwhile, the  $60^{\circ}\text{C}$  shifted cell, which had already undergone substantial capacity loss, was unable to be cycled at the same 1C rate. Therefore, it was cycled at C/10, at which it experienced a brief increase in the

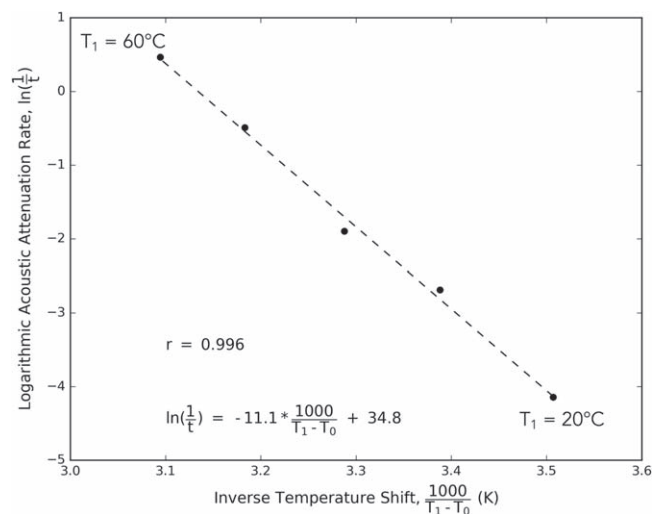


**Figure 3.** Arrhenius relationship between acoustic attenuation rate and inverse temperature shift. The linear trend between logarithmic attenuation rate and inverse temperature is depicted. Higher temperature shifts result in faster signal attenuation rate, which is a clear indicator of substantial gassing in the cell. The correlation coefficient of the trend is 99.6%.

capacity to 0.06 Ah, before falling to 0.04 Ah after 100 cycles (SI Fig. 3b). For comparison, the 0 °C to 20 °C was also cycled at C/10, which netted a markedly improved capacity of 0.15 Ah (SI Fig. 4). Diffusivity tests of the two cells showed overall lower diffusivity coefficients than other cells that did not cycle in cold temperatures (SI Fig. 5). This is especially noted in the “voltage tail” between 3.9 V and 4.2 V, where the values are much lower for the shifted cells as opposed to the non-temperature-shifted cell. Additionally, the starting voltage for the 60 °C shifted cell is much higher than for the other two cells, suggesting an additional degree of degradation. The collection of these results suggests that the temperature shift and associated gassing/loss of signal could be caused by degradation of the liquid electrolyte, as the depleted electrolyte is a likely explanation for the drop in diffusivity values.

After observing these differences between the 20 °C and 60 °C shifted cells, the acoustic effects of a 20 °C to 60 °C shift, and of a constant 60 °C environment were tested (Figs. 4a–4b). The constant 60 °C cycled cell confirmed that a constant high temperature of 60 °C does not cause signal attenuation (Fig. 4a). Therefore, the shift in temperature is vital to the gassing occurrence, rather than simply cycling at the elevated temperature. The 20 °C to 60 °C shift also led to signal loss, suggesting occurrence of gas formation (Fig. 4b). However, unlike the <10 °C to 60 °C shift, the 20 °C to 60 °C shift does not lead to a drop in capacity upon cycling, suggesting that even though gas was formed, it did not lead to catastrophic failure (SI Fig. 6). Even though there was significant gassing, as observed by the outward bulge of the pouch cell, the signal eventually returned after some time. The 0 °C to 20 °C and the 0 °C to 60 °C batteries never showed the same signal recovery, despite re-adjusting the transducers on numerous occasions or attempting to apply more contact pressure, thus showing the extent of the gas formation in those situations.

The acoustic signal attenuation in the cells shifted from cold to higher temperatures (20 °C and to a greater extent, 60 °C), combined with the retention of the acoustic signal in a cell solely cycled at 60 °C, suggests that some electrochemical event that occurred in the cycling at lower temperatures leads to gassing at higher temperatures. To further investigate this, cells were cycled at 0 °C and 20 °C at a slower current rate of C/10 for 10 cycles, before being transitioned to a 60 °C environment.

During the initial cycling at C/10, the cell at 0 °C showed a stable capacity of close to 0.20 Ah (SI Fig. 7), while the cell at 20 °C had a capacity closer to 0.22 Ah (SI Fig. 8). When the cells were transitioned to the 60 °C environment following the initial C/10 cycling, the ToF increased, while the amplitude of the signal dropped (Figs. 4c–4d). This was to be expected: ToF is proportional to the speed of sound, which in this case, decreases as the material temperature increases. However, unlike the batteries that had been cycled at a faster 1C rate with CCCV protocol prior to the transition to higher temperature, these batteries did not lose their acoustic signal, or show much visual evidence of gassing under open circuit voltage. Following the temperature shift to 60 °C and stability in the 60 °C environment, the cells were then cycled at a current rate of 1C CCCV. The acoustic signal is also preserved once cycling at 1C

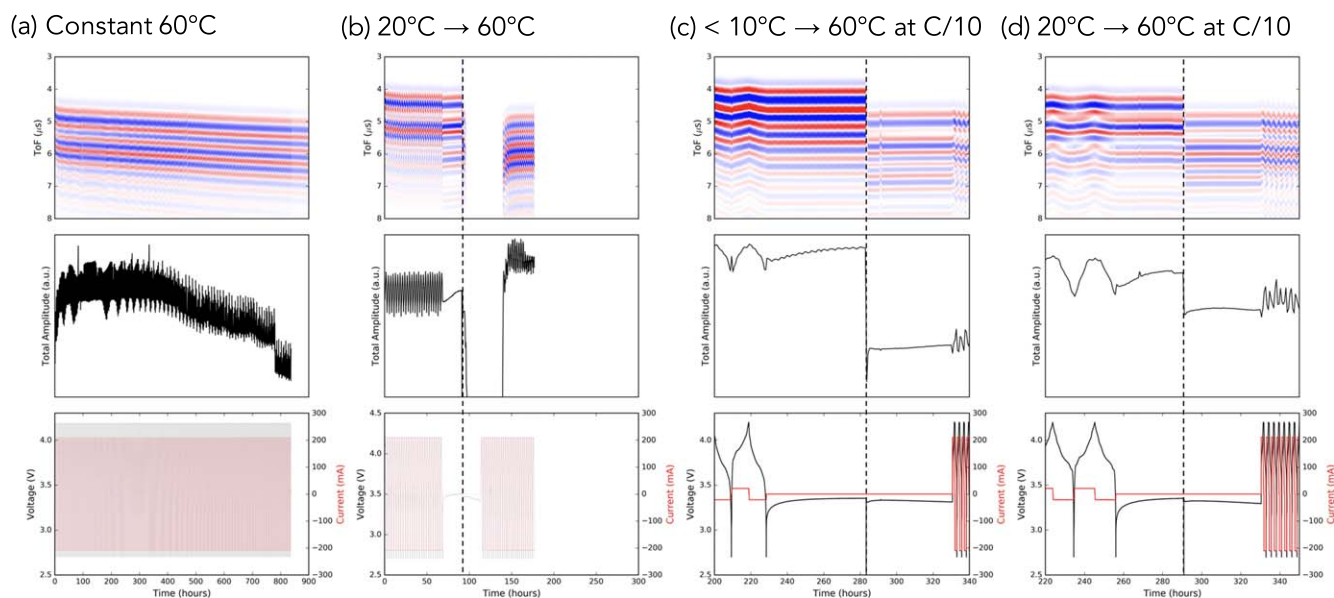


**Figure 4.** Acoustic and electrochemical data for (a) 210 mAh pouch cell cycled at a constant temperature of 60 °C, (b) cell cycled in 20 °C and then shifted to 60 °C at open circuit potential and bottom-of-charge, (c) cell cycled in <10 °C at C/10 and then shifted to 60 °C, and (d) cell cycled in 20 °C at C/10 and then shifted to 60 °C. Note that constant cycling at high temperature does not result in signal attenuation even after almost 900 h of recorded data. The 20 °C to 60 °C shift results in temporary signal recovery followed by permanent attenuation. Cycling at slow C/10 rates in the initial low temperature environments does not result in signal attenuation.

CCCV commences, indicating that minimal damage or gassing occurs. This is in contrast to the cells that were cycled at a faster rate of 1C at the low temperature before the similar transition to a warmer temperature. At a slower C/10 rate, lithium plating is mitigated at the same cold temperature because of minimized mass transport issues. During the subsequent higher temperature shift, there is less plated lithium to react. Therefore, a slower C/10 rate at the initial low temperature may be a method to prevent catastrophic failure upon shifting to a higher temperature environment.

The sum of these acoustic results leads to a few conclusions. First, the attenuation of the signal in all the temperature transitions is accompanied by visible gassing, and happens under open circuit voltage and at 0% SOC. This precludes SEI formation during cycling as the reason for gassing, and also eliminates the effect of being at 100% SOC, which is known to lead to gassing effects. Second, the kinetics of the signal attenuation is highly dependent on the temperature environment the battery is transitioned to.

As such, we can surmise that: (1) the acoustic signal attenuates due to gas formation, (2) the gas formation is dependent on temperature, and (3) the gas formation results from a reaction enabled by a high rate/low temperature electrochemical event. Cells placed in a 60 °C environment without cycling, or cycled at low current rates with a <10 °C to 60 °C transition, did not experience gassing. This behavior is similar to what had been observed by Waldmann et al. who demonstrated that cycling at low temperatures led to Li-metal plating, which then resulted in premature exothermic reactions during accelerated rate calorimetry tests (ARC).<sup>5,31</sup> The transition from 20 °C to 60 °C presents an anomalous case, as the acoustic signal is lost, yet the cell maintains performance. With regards to this transition, we surmise that a small amount of Li was also deposited during cycling in 20 °C and reacted at higher temperature to cause signal loss, but not to a degree that would cause catastrophic cell failure.

**Surface chemical effects of temperature shifts.**—It is known that cycling at colder temperatures can induce lithium plating during the charging step if higher currents are used.<sup>32</sup> This is demonstrated by scanning electron microscopy (SEM) images of graphite anodes after 1C CCCV cycling (SI Fig. 8). As depicted, the graphite anodes cycled at 0 °C show definite lithium plating, with a gray film corresponding to dendrite-like features on the surface in the SEM (SI Figs. 9e–9f). This can be contrasted with graphite cycled at 20 °C, which appeared black without evidence of plating in the SEM (SI Figs. 9a–9b). We suspect that some of the plated lithium at 0 °C proceeds to react with the electrolyte once the cell is transitioned to 60 °C, as electrolyte decomposition reactions are favored by the higher temperature. This would explain the rapid attenuation of the acoustic signal when moved to the 60 °C environment, as opposed to the more gradual degradation when moved to the 20 °C one. However, not all the plated lithium reacts as they are still visible in the SEM (SI Figs. 9c–9d).

To correlate the visual evidence of cold temperature plating with chemical composition changes, post mortem chemical composition analysis of the graphite SEI was conducted with XPS. Figure 5 depicts XPS spectra of the surface and of subsequent depth profiling of three samples: a lithiated graphite anode that was cycled at 0 °C at slow C/10 rate (Fig. 5a), a graphite anode that was cycled at 0 °C at 1C rate (Fig. 5b), and a graphite anode that was cycled in the 0 °C to 60 °C condition also at 1C rate (Fig. 5c). There are two primary observations. First, the graphite anode cycled at a slower C/10 rate and at 0 °C exhibits the strong C-C graphite peak at 285.0 eV after depth profiling; such a strong signal was not observed for the anodes cycled at faster 1C rate. This indicates that the SEI of the faster rate cycled anodes is thicker, as a similar depth profile is unable to detect as much graphite underneath. More importantly, there are consistently higher binding energy peaks for the 0 °C cycled at 1C for all elemental scans (Fig. 5b). The peaks at 536.0 eV in the O 1s scan, at 292.5 eV in the C 1s scan, and at 58.1 eV in the Li 1s scan correlate with the presence of Li<sub>2</sub>CO<sub>3</sub>.<sup>33</sup> The peak at 689.5 eV correlates with

a C-F bond degradation product of LiPF<sub>6</sub>. These are in addition to other peaks that are also observed in the anode cycled at C/10, such as PO<sub>4</sub><sup>3-</sup> at 687.5 eV and LiOH at 533.2 eV.<sup>33–35</sup> However, the higher binding energy peaks observed in the cell cycled at 0 °C all disappear in the 0 °C to 60 °C transitioned cell. Particularly, the peaks fitted to C-F in the F 1s scan, and to Li<sub>2</sub>CO<sub>3</sub> in the O 1s, C 1s, and Li 1s scans no longer appear (Fig. 5c). Presumably, the transition to 60 °C caused these higher binding energy species (C-F and Li<sub>2</sub>CO<sub>3</sub>) formed during cycling at cold temperatures to react with the electrolyte and produce gaseous products such as CO<sub>2</sub> and other organic compounds.<sup>35</sup> These are possible components of the out-gassing observed in the cell that went through the 0 °C to 60 °C transition, based on appearance and subsequent disappearance of products formed on the SEI. Further studies utilizing gas chromatography mass spectroscopy (GC-MS) may help elucidate the exact composition of the aforementioned gasses.<sup>36,37</sup> In the current study, we have focused on operando acoustic detection of observed physical changes, and correlation of these results with changes in the chemical composition of the SEI and the degraded electrolyte.

**Analysis of electrolyte from full cells.**—As both the acoustic and surface chemical analyses suggest that electrolyte decomposition due to the high temperature shift of low temperature-induced lithium-plated graphite was the main cause of gassing, we set out to confirm electrolyte degradation. First, pouch cells were fully discharged before being brought into an Argon filled glovebox, stripped of their plastic pouches, and soaked in 5 mL of 1 M LiPF<sub>6</sub> EC:DMC electrolyte. This allows the electrolyte solutions from the cell to mix with an electrolyte of a known concentration and chemical signature, such that any changes to the electrolyte must have come from the mixing of the known electrolyte, and the electrolyte within the cell.

From Figs. 6a–6d, it is immediately clear that changes have occurred in the previously pure 1 M LiPF<sub>6</sub> EC:DMC electrolyte. When a new cell (Fig. 6a) and one cycled 600 times at 20 °C (Fig. 6b) were placed in the electrolyte bath, almost no color change occurred. The electrolyte bath from a battery that had undergone the 0 °C to 60 °C shift, however, turned dark yellow (Fig. 6c). The extracted electrolyte from a cell which had been purposely over-charged, a well-documented phenomenon known to lead to gassing, electrolyte degradation,<sup>38,39</sup> and cell failure (Fig. 6d), was an even darker shade of yellow.

The color change, or lack thereof, from the electrolytes above indicates the degree of compositional change experienced by the electrolytes during the various cycling procedures and temperatures they were exposed to. The four different electrolytes were characterized by Raman spectroscopy to ascertain the change in electrolyte composition. The Raman spectrum of the new cell shows the two main signatures of the EC molecule: a ring bending mode around 720 cm<sup>-1</sup> and a ring breathing mode around 900 cm<sup>-1</sup>, with those bands moving to slightly higher wavenumbers as lithium ions are increasingly coordinated (Fig. 6g).<sup>40–42</sup> The other peak of interest is the minor peak around 745 cm<sup>-1</sup>, which represents the stretching mode of the PF<sub>6</sub><sup>-</sup> molecule.<sup>43–45</sup> These three peaks of interest are shown with greater resolution in Figs. 6e and 6f. The electrolyte from the cell that was cycled at 1C CCCV for 600 cycles at 20 °C exhibits a nearly identical Raman spectrum as the uncycled electrolyte. The overlap in the spectra implies that the condition of the electrolytes in the new cell and in the cycled cell at 20 °C is very similar. If the electrolyte in the cycled cell had been damaged, we would have expected it to leach into the surrounding electrolyte bath, which would have changed the Raman spectra. The second observation is that the SEI that formed on the cycled cell is not very soluble, as a soluble SEI would have also leached into the surrounding electrolyte. Furthermore, there was plenty of time for leaching to occur, as both batteries were placed in the electrolyte solution for a period of over six months.

On the other hand, electrolytes from the 0 °C to 60 °C shift exhibit a drastic change in the Raman spectra. Unlike the two



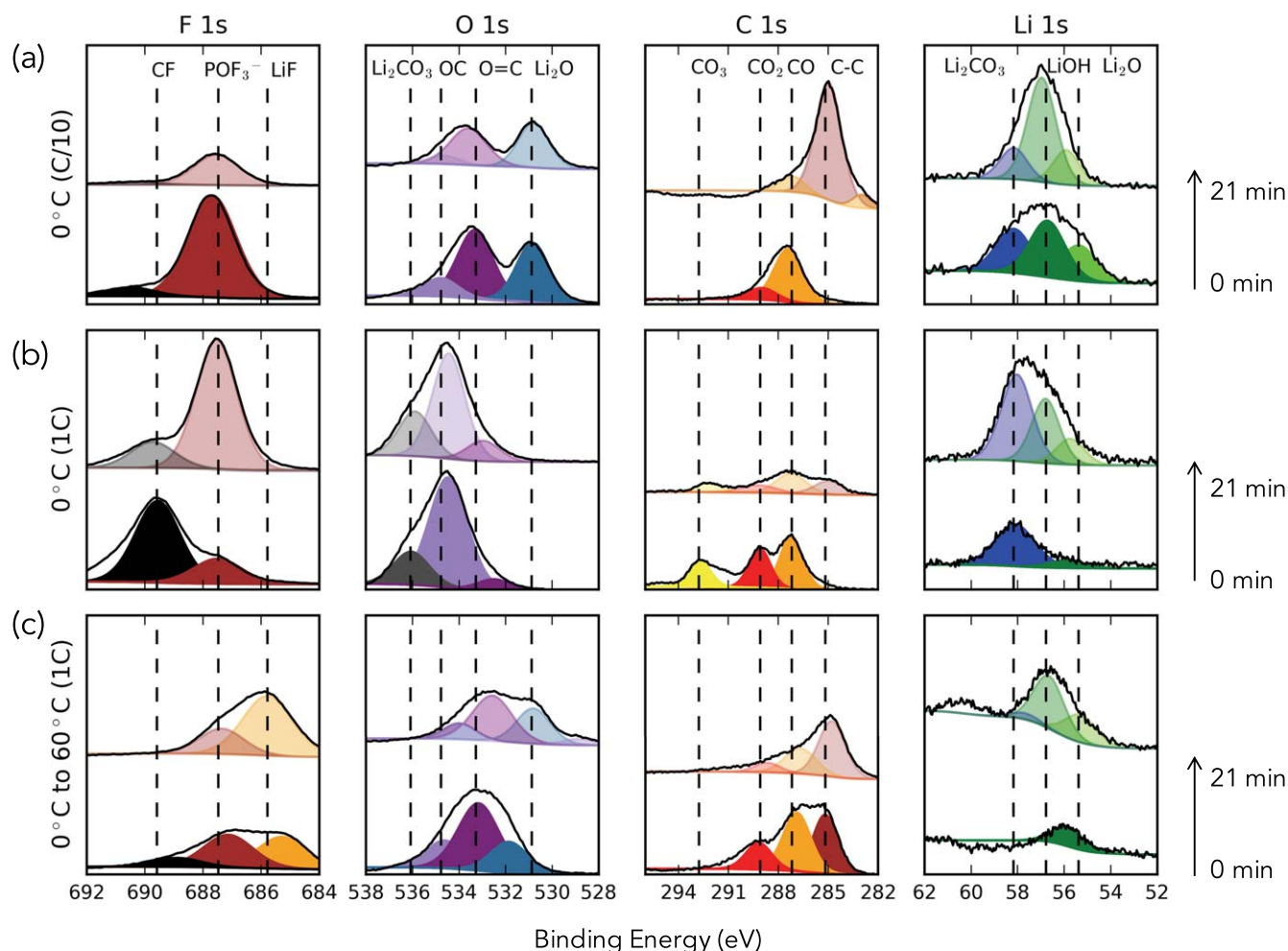


**Figure 5.** XPS spectra (F 1s, O 1s, C 1s, and Li 1s scans) of the graphite anode after (a) cycling at 0 °C, C/10 rate, at 100% SOC; (b) cycling at 0 °C, 1C rate, at 0% SOC; and (c) cycling at 0 °C followed by transition to 60 °C, 1C rate, and at 0% SOC. For each plot, the darker colored bottom spectrum indicates the initial surface scan, and the corresponding lighter colored top spectrum indicates the depth profile scan after 21 min of etching. Y-axis is intensity in counts per second (arbitrary units) and x-axis is binding energy in eV. Point scans were taken with 400  $\mu\text{m}$  spot size and 0.05 eV step size, and depth profile was conducted with a 2 keV monatomic Ar-ion gun for a total of 7 etch cycles at 3 min each.

aforementioned spectra, there are significantly attenuated peaks at  $720\text{ cm}^{-1}$  and  $900\text{ cm}^{-1}$ , while the peak at  $746\text{ cm}^{-1}$  shows a much greater prominence. Additionally, the peaks at  $720\text{ cm}^{-1}$  and  $900\text{ cm}^{-1}$  are now convoluted into two separate peaks. For the  $720\text{ cm}^{-1}$  peak, we can see the appearance of a shoulder peak close to  $730\text{ cm}^{-1}$ , while the  $900\text{ cm}^{-1}$  peak effectively separates into two different peaks: one at  $895\text{ cm}^{-1}$ , and another closer to  $905\text{ cm}^{-1}$ . The shift to a higher wavenumber for both the  $720\text{ cm}^{-1}$  and the  $900\text{ cm}^{-1}$  peaks is due to the presence of a  $\text{Li}^+$  ion coordinated with the EC molecule. As such, the EC- $\text{Li}^+$  ring bending mode is closer to the  $730\text{ cm}^{-1}$ , while the EC- $\text{Li}^+$  ring breathing mode is closer to  $905\text{ cm}^{-1}$ . This indicates that the electrolyte solution from the 0 °C to 60 °C transition case has either a much greater concentration of Li than the other solutions, a reduced concentration of pristine EC molecules, or a combination of both. We postulate that, at low temperatures, lithium was plated on the graphite anode while migrating from the cathode. Once brought to a higher temperature, some of the surface plated lithium then reacted with EC in the electrolyte, to progressively passivate the surface. The byproduct of this reaction is soluble in EC, which is why the breakdown products were able to leach into the pristine electrolyte and increase the lithium concentration. This is also confirmed in the XPS spectra by the complete disappearance of the high binding energy species which had appeared in the 0 °C cycled cell, and the subsequent low lithium counts observed in the SEI for the 0 °C to 60 °C case.

The gas formation and electrolyte breakdown stemming from the low to high temperature shift suggest a parallel to the degradation mechanisms that occur during battery overcharging: lithium metal deposits on the surface of the graphite anode and a significant increase in impedance is observed. When repeating the same electrolyte extraction procedure with an overcharged cell, the electrolyte takes on a substantially darker color. This parallel between the temperature shifted cell and the overcharged cell thus provides strong evidence of the mechanistic similarity between the two conditions.

The set of four electrolytes was also characterized with Fourier Transform Infrared Spectroscopy (FTIR), as shown in Fig. 6h. The new electrolyte and the electrolyte cycled at 20 °C showed nearly identical profiles, as we observed with their corresponding Raman spectra. This further confirms that under normal cycling conditions and at normal temperatures, electrolyte does not degrade. However, we do see a significant change in the FTIR spectra with the overcharged and the 0 °C to 60 °C electrolyte.

Notably, the peak for the damaged electrolytes at  $1800\text{ cm}^{-1}$  decreases in adsorption intensity, while the neighboring peak at  $1750\text{ cm}^{-1}$  remains similar. The peaks in this region represent the C=O stretching mode, and in the case of  $\text{LiPF}_6\text{ EC:DMC}$  a lower ratio of  $1800\text{ cm}^{-1}$  to  $1750\text{ cm}^{-1}$  peak intensity is sign of an increased Li concentration in the electrolyte,<sup>34,46,47</sup> which mirrors the observations made with the Raman results. Additionally, there is a stronger adsorption peak for the damaged electrolytes at  $844\text{ cm}^{-1}$ , which



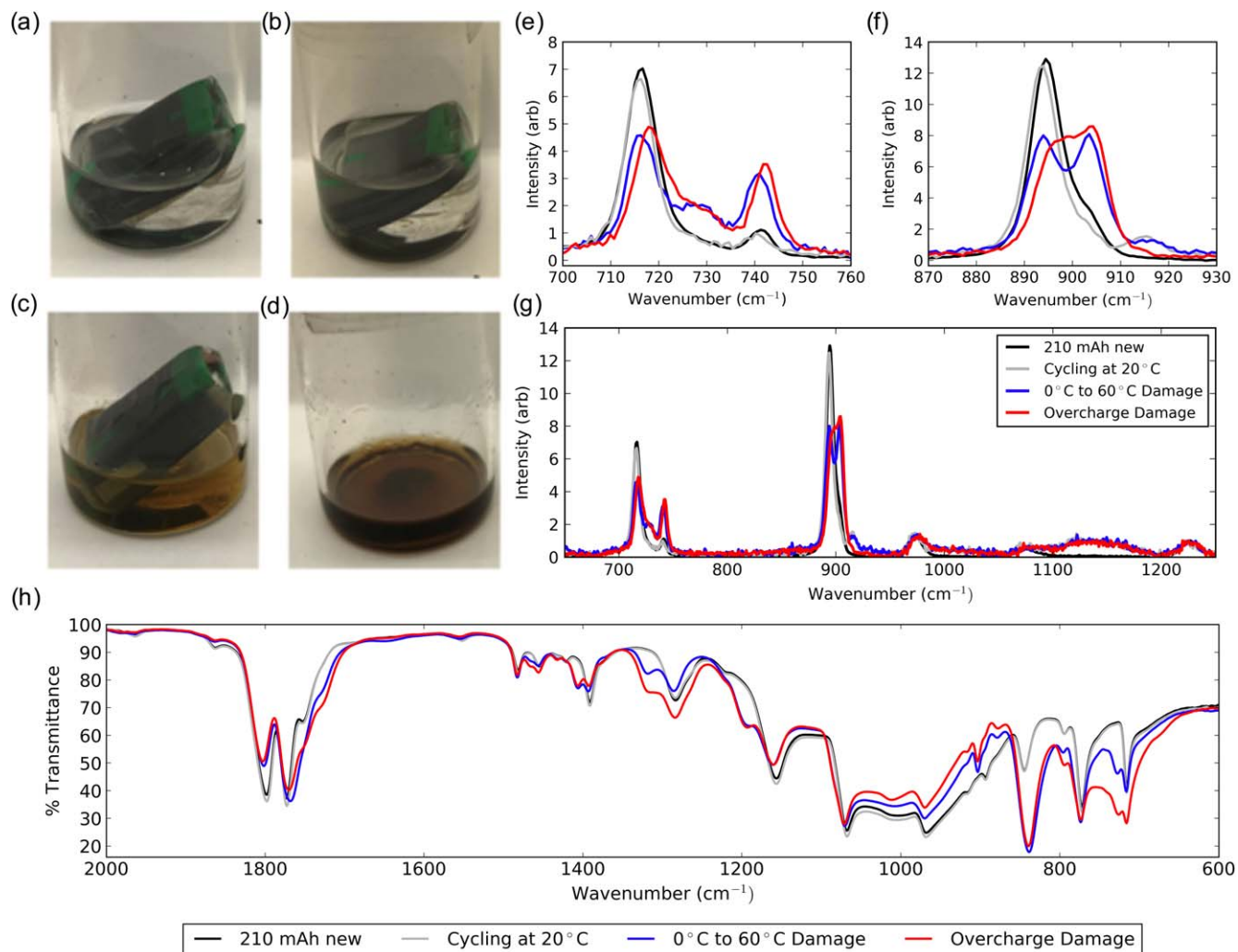


**Figure 6.** Optical images of 1 M LiPF<sub>6</sub> in EC:DMC electrolyte from (a) the new and uncycled 210 mAh cell; (b) the 210 mAh cell after 600 cycles at 20 °C; (c) a cell with apparent gassing after cycling with 20 °C to 60 °C transition; (d) electrolyte flushed from a cell that was overcharged; (e) expanded detail of the EC ring-bending mode around 720 cm<sup>-1</sup>, along with the PF<sub>6</sub><sup>-</sup> symmetric stretch around 740 cm<sup>-1</sup>; (f) expanded detail of the EC ring-stretching mode around 900 cm<sup>-1</sup>; (g) full Raman spectra of the electrolytes shown in (a–d). Raman plots have been normalized according to the C–H stretch, which is represented by the peak at 1220 cm<sup>-1</sup>. The Raman spectra show that the damaged overcharged electrolyte exhibits a slightly more pronounced peak splitting of the 720 cm<sup>-1</sup> and 900 cm<sup>-1</sup> peaks, along with a more prominent 745 cm<sup>-1</sup> stretching band (compared with the 0 °C to 60 °C damaged electrolyte). (h) FTIR spectra of the same electrolytes.

corresponds to the LiPF<sub>6</sub>, thus implying the higher concentration.<sup>48</sup> Lastly, small peaks develop at 1150 cm<sup>-1</sup> [ν(C–O)s], and 1405 cm<sup>-1</sup> [δCH<sub>2</sub>(sc)], for the damaged electrolytes.<sup>49,50</sup> These peaks are all secondary bands stemming from the increased presence of Li<sup>+</sup> in the electrolyte. The decreased prominence of those bands in the damaged electrolyte thus implies the decreased presence of EC in the electrolyte, as some must have invariably been consumed during side reactions catalyzed by the cycling/temperature shift or overcharge.

The similarities in the Raman and FTIR spectra of both types of damaged electrolytes suggest that cycling cells in low temperatures and high currents followed by transitions to high temperature lead to deleterious effects for the battery: lithium plating which then catalyzes subsequent degradation of the electrolyte when brought to higher temperatures. Thus, it is of critical importance for BMS systems to avoid situations that could result in Li-deposition/Li-rich SEI layers, events that can easily happen at temperatures under 10 °C, especially if those batteries are to be exposed to temperatures above 20 °C. Such a variation in temperature is a feature of many climate regions.

**Electrolyte replacement strategy.**—The temperature shift induced gassing and catastrophic loss of cell performance was prevented by implementing a slower C/10 cycling protocol during

the low temperature. Reduced plating at the slower rate led to less decomposition reactions occurring during the shift to higher temperature. Because plating is irreversible, we explored a second strategy of full electrolyte replacement to mitigate gassing due to temperature shifts. To replace the electrolyte, a clean hypodermic needed was used to make two small indentures in the pouch, with 1 M LiPF<sub>6</sub> EC:DMC (1:1) electrolyte injected into the cell. The procedure was repeated at least three times to ensure complete flushing and rejuvenation of the old electrolyte.

The effect of electrolyte replacement of the 0 °C to 60 °C shifted cell was analyzed via capacity and diffusivity measurements. As indicated in Fig. 1, the 0 °C to 60 °C shift during cycling causes a dramatic decrease in the cell capacity. As also shown in Fig. 7c, the capacity falls from 0.22 Ah (black) to 0.084 Ah (gray). The large diffusivity trough around 3.8 V (Fig. 7a) as depicted in GITT also disappears completely, suggesting that lithium storage capabilities at that state of charge are no longer electrochemically accessible in the degraded electrolyte. Average diffusivity values above 3.9 V are also significantly lower than for a fresh cell. After electrolyte replacement, the total cell capacity increased from 0.084 Ah to 0.137 Ah (Fig. 7c, red). While still quite short of the nominal capacity of 0.21 Ah, electrolyte replacement did manage to recover close to 20%

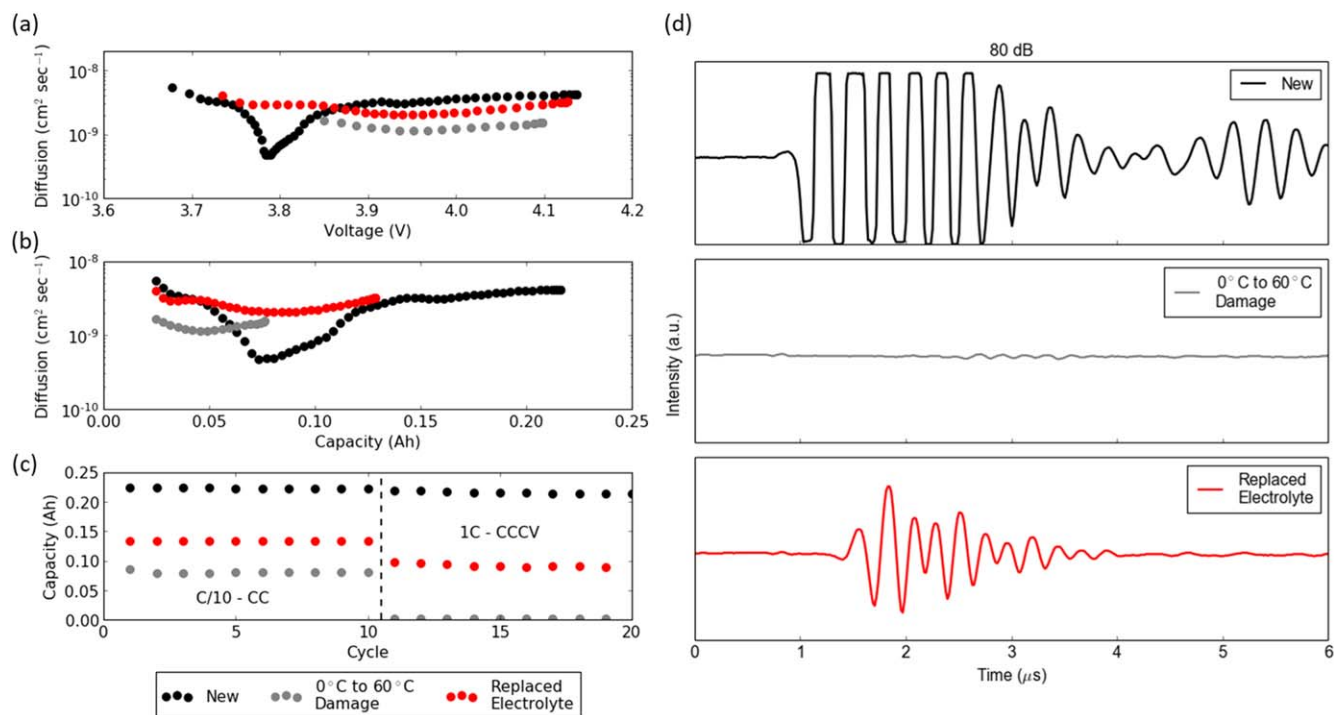


**Figure 7.** (a) GITT diffusivity vs voltage of fresh 210 mAh cell (black), damaged cell from 0 °C to 60 °C shift (gray), and damaged cell from 0 °C to 60 °C shift with electrolyte replaced (red); (b) GITT diffusivity of same 3 cells vs capacity; (c) capacity of the three cells at C/10 (CC) for 10 cycles followed by 1C (CCCV) for 10 cycles; (d) acoustic waveform snapshots at a gain of 80 dB, resulting in oversaturated signal for the fresh cell, completely attenuated signal for the damaged cell, and signal present for the subsequently replaced electrolyte.

of the total cell capacity. Additionally, diffusivity values in the upper voltage plateau are higher than before electrolyte replacement, though still lower than a fresh cell. While replacing the electrolyte does improve cell health with regards to capacity and diffusivity, it cannot fully restore a cell to its pristine condition.

Aside from marginal recovery of the diffusivity and capacity, electrolyte replacement also affects the acoustic properties of the battery. As discussed earlier, the 0 °C to 60 °C shift led to complete loss of acoustic signal due to significant cell gassing. To determine the extent of these losses, additional single pulse acoustic measurements were taken using higher gain (80 dB) and at the bottom of charge (Fig. 7d). For the fresh cell, the acoustic signal has no issue transmitting across the cell, with an oversaturated signal causing waveform cutoffs. For the damaged cell from the temperature shift, only a trace of the acoustic signal remains, despite adequate spring pressure applied to the transducers in order to maintain contact with the cell. Even with insurance of good contact and a higher gain that amounts to a saturated signal in a fresh cell, barely any signal was observed in the damaged cell. There is partial recovery of this signal with the replaced electrolyte. The reappearance of the signal provides some insight into the type of damage created by the temperature shift. Gas pockets between the individual electrode layers would have caused signal attenuation. The cell electrolyte replacement most likely flooded these gas pockets as well as removed soluble components of the degraded SEI/electrolyte, leading to improved contact between electrodes. Therefore, the acoustic waves became less impeded and showed a stronger signal.

### Conclusions

This study demonstrates that charging LCO/Gr pouch cell batteries at a combination of low temperatures and higher current rates is especially catastrophic for battery performance. The combination of plated lithium metal, which typically occurs below 10 °C, and a shift to high temperatures (>20 °C) can lead to extensive gassing and catastrophic failure even if the battery is held at open circuit potential at bottom-of-charge. The occurrence of gassing was determined for

shifts to various temperatures ranging from 20 °C to 60 °C, which led to a statistically significant Arrhenius relationship between rate of signal attenuation and magnitude of temperature shift. Acoustic signal attenuation proved to be an effective parameter for determining when substantial gassing occurred, which was then correlated with post mortem chemical analysis of the SEI and electrolyte. It was shown that lithium deposition at <20 °C is correlated with an increase in high binding energy components in the SEI such as lithium carbonate, which disappear after cycling in 60 °C. Further, Raman and FTIR showed indications of higher amounts of lithium ions in the electrolyte; the continued reaction of the Li-rich SEI formed at 0 °C may lead to gassing observed at 60 °C. Even fairly innocuous temperatures and current rates, such as a 1C charge at 20 °C, can lead to the formation of these deposits. Moreover, this two-step process of lithium deposition followed by lithium reaction can easily be avoided through optimized cycling protocols. Using C/10 charge rates at lower temperatures, before transitioning the battery to a higher temperature environment, led to no immediate gassing or subsequent failure. Cycling a battery at a current rate of 1C exclusively at higher temperatures also managed to avoid all immediate gassing and failure problems. Finally, replacing the low to high temperature shift damaged electrolyte caused reappearance of the acoustic signal due to removal of gas and temporarily improved capacity.

These findings highlight a key relationship between current rate, temperature, lithium deposition and lithium reaction with electrolyte. Poor combinations of these factors can lead to catastrophic failure. These results encourage further research on temperature shift effects in other LIB chemistries and geometries to determine the proper parameter controls that reduce the risk of cell failure.

### Acknowledgments

The authors acknowledge the use of Princeton's Imaging and Analysis Center, which is partially supported by the Princeton Center for Complex Materials, a National Science Foundation (NSF)-MRSEC program (DMR-1420541). D.S., C.B. and W.C. designed the experiments and performed the electrochemical/acoustic

measurements. T.F., J.Y., and S.P. assisted in the collection of the electrochemical data and cell disassembly. D.S. supervised the project. Funding Sources including a gift from Ford Motor Company and cells provided by the Department of Energy Vehicle Technologies Office XCEL Program from Idaho National Lab. Thanks to Eric Dufek, Tanvir Tanim and Skrikant Nagpure for insightful conversations. D.S. is a founder of Feasible, which employs the ultrasonic technique (patent application #20160223498) used herein. Feasible did not fund the work nor participate in its execution.

## References

1. M. T. F. Rodrigues, G. Babu, H. Gullapalli, K. Kalaga, F. N. Sayed, K. Kato, J. Joyner, and P. M. Ajayan, "A materials perspective on li-ion batteries at extreme temperatures." *Nat. Energy*, **2**, 17108 (2017).
2. G. Sarre, P. Blanchard, and M. Broussely, "Aging of lithium-ion batteries." *J. Power Sources*, **127**, 65 (2004).
3. M. Dubarry, N. Qin, and P. Brooker, "Calendar aging of commercial li-ion cells of different chemistries—a review." *Curr. Opin. Electrochem.*, **9**, 106 (2018).
4. F. Leng, C. M. Tan, and M. Pecht, "Effect of temperature on the aging rate of li ion battery operating above room temperature." *Sci. Rep.*, **5**, 12967 (2015).
5. M. Fleischhammer, T. Waldmann, G. Bisle, B. I. Hogg, and M. Wohlfahrt-Mehrens, "Interaction of cyclic ageing at high-rate and low temperatures and safety in lithium-ion batteries." *J. Power Sources*, **274**, 432 (2015).
6. M. Ouyang, Z. Chu, L. Lu, J. Li, X. Han, X. Feng, and G. Liu, "Low temperature aging mechanism identification and lithium deposition in a large format lithium iron phosphate battery for different charge profiles." *J. Power Sources*, **286**, 309 (2015).
7. S. S. Zhang, K. Xu, and T. R. Jow, "Low temperature performance of graphite electrode in li-ion cells." *Electrochim. Acta*, **48**, 241 (2002).
8. S. F. Schuster, T. Bach, E. Fleder, J. Müller, M. Brand, G. Sextl, and A. Jossen, "Nonlinear aging characteristics of lithium-ion cells under different operational conditions." *J. Energy Storage*, **1**, 44 (2015).
9. S. Nowak and M. Winter, "Review—chemical analysis for a better understanding of aging and degradation mechanisms of non-aqueous electrolytes for lithium ion batteries: method development, application and lessons learned." *J. Electrochem. Soc.*, **162**, A2500 (2015).
10. T. Waldmann, M. Wilka, M. Kasper, M. Fleischhammer, and M. Wohlfahrt-Mehrens, "Temperature dependent ageing mechanisms in lithium-ion batteries—a post-mortem study." *J. Power Sources*, **262**, 129 (2014).
11. M. S. D. Darma, M. Lang, K. Kleiner, L. Mereacre, V. Liebau, F. Fauth, T. Bergfeldt, and H. Ehrenberg, "The influence of cycling temperature and cycling rate on the phase specific degradation of a positive electrode in lithium ion batteries: a post mortem analysis." *J. Power Sources*, **327**, 714 (2016).
12. M. Rosa Palacín, "Understanding ageing in li-ion batteries: a chemical issue." *Chem. Soc. Rev.*, **47**, 4924 (2018).
13. J. Xia, L. Ma, and J. R. Dahn, "Improving the long-term cycling performance of lithium-ion batteries at elevated temperature with electrolyte additives." *J. Power Sources*, **287**, 377 (2015).
14. A. J. Smith, H. M. Dahn, J. C. Burns, J. C., and J. R. Dahn, "Long-term low-rate cycling of LiCoO<sub>2</sub>/Graphite li-ion cells at 55 °C." *J. Electrochem. Soc.*, **159**, A705 (2012).
15. M. Ecker, N. Nieto, S. Käbitz, J. Schmalstieg, H. Blanke, A. Warnecke, and D. U. Sauer, "Calendar and cycle life study of li(NiMnCo)O<sub>2</sub>-based 18650 lithium-ion batteries." *J. Power Sources*, **248**, 839 (2014).
16. C. Campion, W. Li, and B. Lucht, "Thermal decomposition of LiPF<sub>6</sub>-Based electrolytes for lithium-ion batteries." *J. Electrochem. Soc.*, **152**, A2327 (2005).
17. Y. Fernandes, A. Bry, and S. de Persis, "Identification and quantification of gases emitted during abuse tests by overcharge of a commercial li-ion battery." *J. Power Sources*, **389**, 106 (2018).
18. Y. Fernandes, A. Bry, and S. de Persis, "Thermal degradation analyses of carbonate solvents used in li-ion batteries." *J. Power Sources*, **414**, 250 (2019).
19. Y. Zheng, K. Qian, D. Luo, Y. Li, Q. Lu, B. Li, Y. B. He, X. Wang, J. Li, and F. Kang, "Influence of over-discharge on the lifetime and performance of LiFePO<sub>4</sub>/graphite batteries." *RSC Adv.*, **6**, 30474 (2016).
20. N. S. Spinner, C. R. Field, M. H. Hammond, B. A. Williams, K. M. Myers, A. L. Lubrano, S. L. Rose-Pehrson, and S. G. Tuttle, "Physical and chemical analysis of lithium-ion battery cell-to-cell failure events inside custom fire chamber." *J. Power Sources*, **279**, 713 (2015).
21. D. P. Finegan, E. Darcy, M. Keyser, B. Tjaden, T. M. M. Heenan, R. Jervis, J. J. Bailey, N. T. Vo, O. V. Magdysyuk, and M. Drakopoulos, "Thermal runaway: identifying the cause of rupture of li-ion batteries during thermal runaway." *Adv. Sci.*, **5**, 1870003 (2018).
22. D. P. Finegan, J. Darst, W. Walker, Q. Li, C. Yang, R. Jervis, T. M. M. Heenan, J. Hack, J. C. Thomas, and A. Rack, "Modelling and experiments to identify high-risk failure scenarios for testing the safety of lithium-ion cells." *J. Power Sources*, **417**, 29 (2019).
23. J. B. Robinson, D. P. Finegan, T. M. M. Heenan, K. Smith, E. Kendrick, D. J. L. Brett, and P. R. Shearing, "Microstructural analysis of the effects of thermal runaway on Li-ion and Na-ion battery electrodes." *J. Electrochem. Energy Convers. Storage*, **15**, 011010 (2017).
24. Q. Q. Liu, D. J. Xiong, R. Petibon, C. Y. Du, and J. R. Dahn, "Gas evolution during unwanted lithium plating in li-ion cells with ec-based or ec-free electrolytes." *J. Electrochem. Soc.*, **163**, A3010 (2016).
25. W. Weppner and R. A. Huggins, "Determination of the kinetic parameters of mixed-conducting electrodes and application to the system Li<sub>3</sub>Sb." *J. Electrochem. Soc.*, **124**, 1569 (1977).
26. D. W. Dees, S. Kawauchi, D. P. Abraham, and J. Prakash, "Analysis of the galvanostatic intermittent titration technique (GITT) as applied to a lithium-ion porous electrode." *J. Power Sources*, **189**, 263 (2009).
27. A. Hsieh, S. Bhadra, B. J. Hertzberg, P. J. Gjeltema, A. W. Goy, J. A. Fleischer, and D. Steingart, "Electrochemical-acoustic time of flight: In operando correlation of physical dynamics with battery charge and health." *Energy Environ. Sci.*, **8**, 1569 (2015).
28. G. Davies, K. W. Knehr, B. V. Tassell, T. Hodson, S. Biswas, A. G. Hsieh, and D. A. Steingart, "State of charge and state of health estimation using electrochemical acoustic time of flight analysis." *J. Electrochem. Soc.*, **164**, A2746 (2017).
29. K. W. Knehr, T. Hodson, C. Bommer, G. Davies, A. Kim, and D. A. Steingart, "Understanding full-cell evolution and non-chemical electrode crosstalk of li-ion batteries." *Joule*, **2**, 1146 (2018).
30. B. P. Matadi, S. Genès, A. Delaille, C. Chabrol, E. de Vito, M. Bardet, J. F. Martin, L. Daniel, and Y. Bultel, "Irreversible capacity loss of li-ion batteries cycled at low temperature due to an untypical layer hindering li diffusion into graphite electrode." *J. Electrochem. Soc.*, **164**, A2374 (2017).
31. T. Waldmann and M. Wohlfahrt-Mehrens, "Effects of rest time after Li plating on safety behavior—ARC tests with commercial high-energy 18650 Li-ion cells." *Electrochim. Acta*, **230**, 454 (2017).
32. J. Vetter, P. Novák, M. R. Wagner, C. Veit, K. C. Möller, J. O. Besenhard, M. Winter, M. Wohlfahrt-Mehrens, C. Vogler, and A. Hammouche, "Ageing mechanisms in lithium-ion batteries." *J. Power Sources*, **147**, 269 (2005).
33. K. N. Wood and G. Teeter, "XPS on Li-battery-related compounds: analysis of inorganic SEI phases and a methodology for charge correction." *ACS Appl. Energy Mater.*, **1**, 4493 (2018).
34. B. Jiang, V. Ponnuchamy, Y. Shen, X. Yang, K. Yuan, V. Vetere, S. Mossa, I. Skarmoutsos, Y. Zhang, and J. Zheng, "The anion effect on Li+ Ion coordination structure in ethylene carbonate solutions." *J. Phys. Chem. Lett.*, **7**, 3554 (2016).
35. B. S. Parimalam, A. D. MacIntosh, R. Kadam, and B. L. Lucht, "Decomposition reactions of anode solid electrolyte interphase (SEI) components with LiPF<sub>6</sub>." *J. Phys. Chem. C*, **121**, 22733 (2017).
36. Z. Mao, M. Farkhondeh, M. Pritzker, M. Fowler, and Z. Chen, "Calendar aging and gas generation in commercial graphite/NMC-LMO lithium-ion pouch cell." *J. Electrochem. Soc.*, **164**, A3469 (2017).
37. C. P. Aiken, J. Xia, D. Y. Wang, D. A. Stevens, S. Trussler, and J. R. Dahn, "An apparatus for the study of In Situ gas evolution in Li-ion pouch cells." *J. Electrochem. Soc.*, **161**, A1548 (2014).
38. K. Kumai, H. Miyashiro, Y. Kobayashi, K. Takei, and R. Ishikawa, "Gas generation mechanism due to electrolyte decomposition in commercial lithium-ion cell." *J. Power Sources*, **81–82**, 715 (1999).
39. R. Imhof and P. Novák, "Oxidative electrolyte solvent degradation in lithium-ion batteries: an In Situ differential electrochemical mass spectrometry investigation." *J. Electrochem. Soc.*, **146**, 1702 (1999).
40. M. Morita, Y. Asai, N. Yoshimoto, and M. Ishikawa, "A raman spectroscopic study of organic electrolyte solutions based on binary solvent systems of ethylene carbonate with low viscosity solvents which dissolve different lithium salts." *J. Chem. Soc. Faraday Trans.*, **94**, 3451 (1998).
41. B. Klassen, R. Aroca, R. M. Nazri, and G. A. Nazri, "Raman spectra and transport properties of lithium perchlorate in ethylene carbonate based binary solvent systems for lithium batteries." *J. Phys. Chem. B*, **102**, 4795 (1998).
42. M. Masia, M. Probst, and R. Rey, "Ethylene carbonate–Li+: A theoretical study of structural and vibrational properties in gas and liquid phases." *J. Phys. Chem. B*, **108**, 2016 (2004).
43. L. Doucey, M. Revault, A. Lautié, A. Chaussé, and R. Messina, "A study of the Li/Li+ couple in DMC and PC solvents: I. Characterization of LiAsF<sub>6</sub>/DMC and LiAsF<sub>6</sub>/PC solutions." *Electrochim. Acta*, **44**, 2371 (1999).
44. R. Aroca, M. Nazri, G. A. Nazri, A. J. Camargo, and M. Trsic, "Vibrational spectra and ion-pair properties of lithium hexafluorophosphate in ethylene carbonate based mixed-solvent systems for lithium batteries." *J. Solut. Chem.*, **29**, 1047 (2000).
45. C. M. Burba and R. Frech, "Spectroscopic measurements of ionic association in solutions of LiPF<sub>6</sub>." *J. Phys. Chem. B*, **109**, 15161 (2005).
46. D. M. Seo, S. Reininger, M. Kutcher, K. Redmond, W. B. Euler, and B. L. Lucht, "Role of mixed solvation and ion pairing in the solution structure of lithium ion battery electrolytes." *J. Phys. Chem. C*, **119**, 14038 (2015).
47. A. V. Cresce et al., "Solvation behavior of carbonate-based electrolytes in sodium ion batteries." *Phys. Chem. Chem. Phys.*, **19**, 574 (2017).
48. M. Nie, D. P. Abraham, D. M. Seo, Y. Chen, A. Bose, and B. L. Lucht, "Role of solution structure in solid electrolyte interphase formation on graphite with LiPF<sub>6</sub> in propylene carbonate." *J. Phys. Chem. C*, **117**, 25381 (2013).
49. P. Lanz and P. Novák, "Combined in situ Raman and IR microscopy at the interface of a single graphite particle with ethylene carbonate/dimethyl carbonate." *J. Electrochem. Soc.*, **161**, A1555 (2014).
50. A. M. Haregewoin, T. D. Shie, S. D. Lin, B. J. Hwang, and F. M. Wang, "An effective In Situ drifts analysis of the solid electrolyte interface in lithium-ion battery." *ECS Trans.*, **53**, 23 (2013).